Received 14 December 2021; revised 20 January 2022; accepted 2 February 2022. Date of publication 7 February 2022; date of current version 14 February 2022.

Digital Object Identifier 10.1109/OJAP.2022.3149392

Dual-Function Triple-Band Heatsink Antenna for Ambient RF and Thermal Energy Harvesting

AZAMAT BAKYTBEKOV[1], THANG Q. NGUYEN[1], GE ZHANG[2], MICHAEL S. STRANO[2], KHALED N. SALAMA[1], AND ATIF SHAMIM[1] (Senior Member, IEEE)

[1]Department of Electrical Engineering, King Abdullah University of Science and Technology, Thuwal 23955, Saudi Arabia

[2]Department of Chemical Engineering, Massachusetts Institute of Technology, Cambridge, MA 02139, USA

CORRESPONDING AUTHOR: A. BAKYTBEKOV (e-mail: azamat.bakytbekov@kaust.edu.sa)

This work was supported by the KAUST Sensor Initiative under Award OSR-2015-Sensors-2700.

ABSTRACT The Internet of Things (IoT) infrastructure requires billions of devices that must ideally be self-powered. Ambient RF and thermal energy have great potential since they are both available continuously throughout the day. An RF harvester is a rectenna that is a combination of a receiving antenna and a rectifier. Thermal energy harvesters (TEH) are typically static type, with a fixed hot source at one end and a cold source at the other. Here, we present a transient type TEH that generates energy from diurnal cycle temperature fluctuations. Smart integration is achieved by designing the antenna to also act as the heatsink for the TEH. The antenna must be optimized while considering the electromagnetic radiation as well as the heat transfer performances. Thus, two simulators, Ansys HFSS and Ansys Fluent, were employed. The antenna operates at GSM900, GSM1800, and 3G bands simultaneously, with measured gains of 3.8, 4, and 5.3 dB, respectively, which have increased by ∼3–4 dB (radiation efficiency doubled from ∼40% to ∼80%) compared to the flat antenna (with no heatsink fins). The TEH is in the form of a square box where two identical rectennas cover the four sides. Through RF field testing, ∼250 mV is consistently collected at any instance (6.25 μW for a 10 kΩ load). Without the heatsink antenna, the average power collected from the TEH is 13.6 μW, which increases by 2.3 times when the heatsink antenna is integrated, highlighting the utility of this co-design and monolithic integration, which enhances both RF and thermal harvested powers.

INDEX TERMS Ambient energy harvester, heatsink antenna, radio frequency (RF) energy harvester, thermal energy harvester, self-powered IoT devices.

I. INTRODUCTION

THE INTERNET of Things (IoT) is a fast-growing global infrastructure of physical objects connected through the Internet. It is estimated that the number of IoT devices will reach 75 billion by 2025 [1]. This massive growth is accompanied by the problem of the huge energy consumption of these devices. The traditional method of powering devices with batteries [2]–[4] may be impractical in the scenario of the IoT since recharging or replacing the batteries is not an ideal solution, especially in remote or hard-to-reach places. Different ambient energy harvesters can be used to power these devices fully or partially to either eliminate batteries or extend the battery lives. Different types of ambient energy harvesters exist, such as solar, thermal, electromagnetic, and mechanical, which can be used to power IoT devices [5]. A single ambient energy source (such as solar) can be used to power these IoT devices, however, solar is not readily available continuously everywhere. Alternative ambient sources can be explored, however, relying on one type of stand-alone ambient energy harvester is a high-risk plan as ambient energy sources are unpredictable. Thus, combining two or several ambient energy harvesters in one module may solve this issue by making the device more versatile. Ambient RF and thermal energy are suitable options for this multi-source harvester concept since both are available continuously throughout the day.

RF energy is not a natural source of energy, unlike solar or wind energy. However, with the development of wireless technologies (GSM, Wi-Fi, LTE 4G and 5G, etc.), wireless signals have become integral to human living environments. Ambient RF energy can be efficiently and continuously collected 24 hours a day through a receiving antenna and a rectifier circuit, typically known as a rectenna. Thermal energy harvesters (TEHs) are typically static type, with a fixed hot source at one end and a cold source at the other end. The TEH in this work is different from the conventional static TEH as it generates electrical energy from the temperature difference between ambient air (diurnal cycle temperature fluctuations) and phase change material (PCM) inside the TEH [6]. In [6], we demonstrated a non-optimized and superficial integration of these harvesters into one module as a proof of concept. However, smart integration is required to 1) use the space efficiently by sharing common components and 2) boost the amount of collected energy by achieving synergy between the two harvesters. A possible solution for better integration is to optimize the receiving antenna of the RF energy harvester (RFEH) to perform a dual function: work as a heatsink for the TEH in addition to its main duty of receiving the electromagnetic (EM) energy. However, the heatsink antenna must be carefully designed so that both RF and thermal performances can be enhanced.

Multi-band RF energy harvesters [7]–[9] and its combination with different type of ambient energy harvesters such as kinetic [10]–[11] and solar [12] have been presented in the literature. In [13]–[14] harvesting from RF and thermal energy sources has been demonstrated. In both works static type TEH, which is a single commercial off-the-shelf thermoelectric (TE), is used to improve the power conversion efficiency (PCE) of the diode rectifier. In turn, RFEH in both works are simple, single-band rectennas at 2.4 GHz. Though, a heatsink is used in [14] which is connected to the ground plane of the patch antenna, co-optimization of the heatsink has not been done since the heatsink is not part of the antenna's radiating element. This kind of concept where the two harvesters, multi-band RFEH and transient TEH, are co-designed by optimization of EM radiation and heat transfer performances through a single component, has never been done before. In fact, heatsink antennas have never been used for ambient energy harvesting applications as part of a rectenna. Only a few published works exist on heatsink antennas [15]–[19], where most of the designs focus on heat dissipation from the integrated circuits (ICs), also known as chips. In the published works, the antenna performance is never optimized from the heat transfer perspective. These papers mainly involve a simple single-band microstrip patch antenna, either integrated with a commercial heatsink or an in-house non-optimized heatsink (fins, sapphire layer, cubes). Thus, neither design trade-offs between the antenna radiation and heat transfer performances nor design guidelines are available for previously published heatsink antennas.

In this paper, we alleviated the above-mentioned shortcomings by carefully designing a dual-purpose heatsink antenna, where the design has been optimized for both EM and thermal performances to demonstrate a novel monolithically integrated multi-source ambient energy harvester. Through this design optimization, both the RFEH as well as the TEH energy collection have been significantly enhanced. The heatsink antenna has been designed using Ansys high-frequency structure simulator (HFSS) from an EM perspective, while the heat transfer optimization has been performed using Ansys Fluent. The heatsink antenna operates on three bands (GSM 900 MHz, GSM 1800 MHz and 3G 2100 MHz) simultaneously. The gain of the heatsink antenna is 3.8 dB, 4 dB, and 5.3 dB for the three bands, respectively, which is an improvement of ∼3–4 dB compared to the flat version of the antenna (without fins). An output voltage of ∼250 mV (6.25 μW) has been harvested consistently across the 10 kΩ load resistor during any instance in the field measurements. The heatsink antennas occupy four sides of the TEH box and boost the time-averaged collected power by 2.3 times (130%), from 13.6 μW to 31.3 μW.

Section II briefly describes the multi-source ambient energy harvester. Section III focuses on the antenna design by studying the RF and thermal performances and trade-offs. Section IV presents the fabrication and characterization of the heatsink antenna. Section V describes the design and fabrication of a rectifier circuit with a triple-band matching network. The field testing results of the ambient RFEH and the TEH are presented and analyzed in Section VI.

II. MULTI-SOURCE ENERGY HARVESTER

The heatsink antenna in this work is designed for the multi-source ambient energy harvester, which consists of the RFEH and the TEH. This section describes how the TEH works, what materials form its body, and the electrical characterization of these materials for the frequencies of interest. This step is essential in creating the HFSS model of the TEH to design the heatsink antenna. The characterization step is challenging due to the complex and multi-material design of the TEH.

A. PROPOSED TEH

Typically, the static TEH modules operate based on the concept of Seebeck effect [20], which requires a spatial temperature gradient (one hot end and one cold end) on two sides of the TE in a specific location. Subsequently, the TE generates electrical energy due to this temperature difference. In this work, the proposed TEH module operates based on a combination of the TEs as well as an accurately selected PCM that, due to its high latent heat (energy released/absorbed during constant-temperature phase change process), can serve as one end of the TE at a constant temperature. The opposite end of the TE employs ambient diurnal air temperature variation as described in (1) [21].

$$T_{amb}(t) = T_0 + T_A \sin(\omega t) \tag{1}$$

where T_{amb}, T_0 *and* T_A are the ambient temperature, the median temperature and the amplitude of ambient temperature fluctuations respectively, ω is the angular frequency

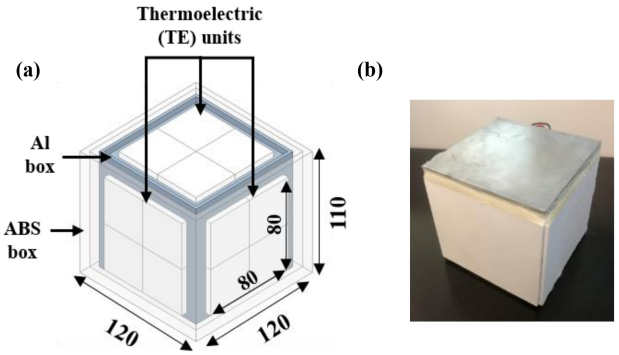

FIGURE 1. (a) HFSS model of the TEH; units: mm (b) Fabricated TEH without fins.

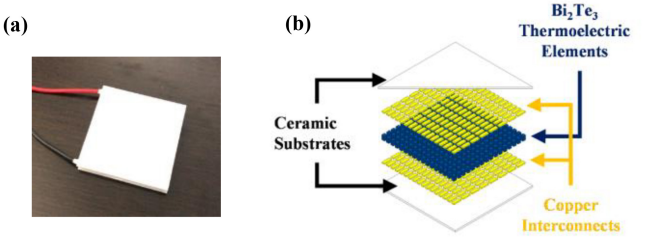

FIGURE 2. (a) Thermoelectric (TE) unit; (b) Exploded view of the thermoelectric (TE) unit.

of temperature fluctuations, t is time. Thus, the PCM must be carefully selected, with the phase-transition temperature close to the midpoint of the day/night temperature extremes of a particular location.

Maximum input and output heat flux of the TEH is given in (2).

$$|J_{MAX}| = eT_A\sqrt{\omega} \tag{2}$$

where e is a very important metric for the TEH performance called thermal effusivity. Average output power of the TEH collected from the ambient environment can be calculated by multiplying the maximum heat flux to the constants such as η efficiency of the TEs and Q performance factor as shown in (3).

$$p_{avg} \approx \eta|J_{MAX}|Q = \eta eT_A\sqrt{\omega}Q \tag{3}$$

In turn, thermal effusivity is given by (4).

$$e = \sqrt{kph} \tag{4}$$

where k is the thermal conductivity, ρ is the density and h is the latent heat per mass.

Fig. 1(a) shows the HFSS model of the TEH. The inner box (shown in grey) made of aluminum (Al) is filled with PCM and nickel foam (Ni). The Al box is used due to its decent thermal conductivity (240 W/m·K) and relatively lower cost. The PCM used in this work is eicosane (E), which has a phase change point at 37°C, enabling it to efficiently generate electrical energy from the day/night temperature fluctuations in Saudi Arabia [21]. Ni helps increase the thermal conductivity of the PCM. In Fig. 1(a), TEs are shown in white. TE with dimensions of 80 mm × 80 mm × 4 mm (4 connected TE units) are placed on the top wall and four sidewalls of the Al box. Finally, the outer box (shown in transparent white), made of ABS (acrylonitrile butadiene styrene), not only protects the TEH but also acts as the substrate for the heatsink antenna. ABS (a plastic material) is selected due to its low loss tangent (0.004) and easy fabrication through 3D printing. A thin ABS wall is preferred for better TEH performance because of the low thermal conductivity of ABS plastic (0.2 W/m·K). However, the RF antenna requires a thicker wall, which will be discussed in detail in Section II-B. As a tradeoff, 5 mm wall thickness is selected, which is a good compromise between the TEH and RF energy harvester performances.

The overall size of the TEH is 120 mm × 120 mm × 110 mm. The fabricated TEH (without fins) is shown in Fig. 1(b), where the Al lid is placed on top of the TEH.

B. RF CHARACTERIZATION OF THE TEH

The TEH comprises four layers of materials: 1) a mixture of Ni/E, 2) Al, 3) TEs, and 4) ABS. Two of them, Al and ABS, have known electrical properties that could be directly used in the EM simulator (Ansys HFSS in our case). However, no data is available in the open literature for a Ni/E mixture and TEs in the GHz range.

Creating an exact model for the Ni foam filled with E in HFSS is a challenging task, which is expected to result in an extremely long simulation time. Since the Ni foam and E mixture is inside the Al box, so from the EM simulations perspective, we could simplify the model in HFSS. This simplification is achieved by assuming that only bulk Ni exists in the Al box. This assumption, which significantly simplifies the EM model, works out well, as shown by a good match between the simulations and measurements (shown later in Section IV).

Characterizing the TE, shown in Fig. 2(a), for the GHz range, is another challenging task due to its complex construction, as shown in its exploded view in Fig. 2(b). It comprises ceramic plates as a cover, copper interconnects, and semiconductor elements made of bismuth telluride (Bi_2Te_3). Creating an HFSS model for the TE and using it in antenna design simulations involves two potential problems: 1) the dielectric constant and loss tangent of the Bi_2Te_3 in the GHz range is unavailable; 2) the EM simulation model becomes extremely complex due to the presence of 20 TEs in the TEH design, which is expected to significantly increase the simulation time. Instead, the TE unit can be considered as a homogeneous black box whose dielectric constant and loss tangent could be extracted through microwave measurements to avoid these issues. For this purpose, a V type dipole antenna, made of copper tape, is designed in HFSS and realized on the fabricated TEH diagonally, as shown in Fig. 3. For the design of the V type antenna on the TEH module, a dielectric permittivity (ε_r) of 5.5 is used as an initial estimate for the TE, which is an average permittivity for the combination of ceramic plates ($\varepsilon_r = 10$ for 96% alumina)

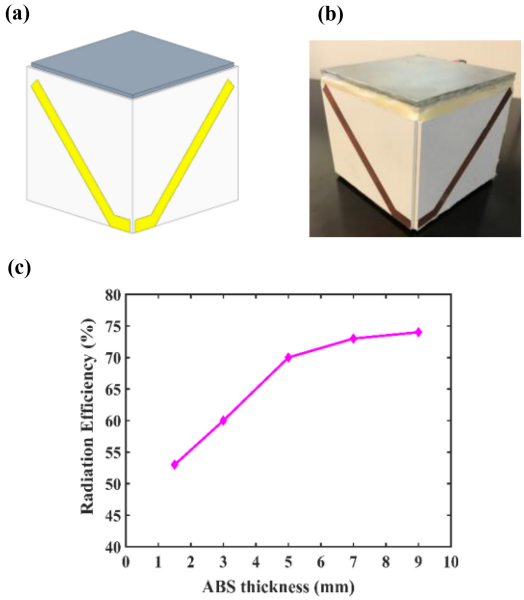

FIGURE 3. (a) HFSS model of copper tape antennas on the TEH (b) Fabricated model of copper tape antennas on the TEH (c) Radiation efficiency of the heatsink antenna as a function of ABS thickness.

TABLE 1. Electrical properties of thermoelectric (TE) units.

Frequency	Dielectric constant	Loss tangent
900 MHz	7.25	0.1
1800 MHz	3	0.2
2100 MHz	1.5	0.23

and air ($\varepsilon_r = 1$). Similarly, a loss tangent (tan δ) value of 0.01 has been used in the EM simulation model as an initial guess. In order to characterize the TE, first the V type dipole is designed for 900 MHz with the estimated εr and tan δ values. The fabricated antenna has been measured with a vector network analyzer (VNA) for its resonance frequency as well as for its gain in an anechoic chamber. The variation in the resonance frequency and gain is due to the error in the initially estimated values of ε_r and tan δ. This error is corrected in the post-simulation results by varying the ε_r and tan δ values until a good match is achieved between the measured and simulated results. The same procedure is adopted for the other intended frequency bands to address dispersion effects (variance in ε_r and tan δ due to frequency). The final values are shown in Table 1, which illustrates a significant dispersion in the TE materials.

As it was mentioned earlier, thicker ABS wall is required for better antenna performance since the body of the TEH consists of lossy components as shown in Table 1. Thus, separating the heatsink antenna from the lossy body of the TEH with thick ABS walls can increase the efficiency of the antenna. As shown in Fig. 3 (c), the radiation efficiency of the antenna improves from 55% to 70% when the ABS thickness is increased up to 5 mm. However, additional thickness does not improve the radiation efficiency significantly since at 9 mm thickness, the radiation efficiency reaches only 73%. Thus, 5 mm ABS thickness is selected. Heat transfer simulations in Ansys Fluent showed that the 5 mm thick ABS wall deteriorates the average collected power from the TEH by 8% which is an acceptable sacrifice considering the big advantage in terms of the radiation efficiency of the antenna. Also, in terms of the mechanical stability and the amount of ABS material usage, 5 mm thickness is considered as a reasonable value.

III. HEATSINK ANTENNA DESIGN

A. DESIGN CONSIDERATIONS FOR THE HEATSINK ANTENNA

Simultaneously harvesting RF energy from several available frequency bands enhances the collected energy since the available ambient RF power is regulated to safe exposure levels in each frequency band. Thus, the available RF power is relatively low compared to other ambient sources. Depending on the distance from the cellular tower and user activity at a particular instance, the RF power can be relatively small. Power measurements around the campus of a university showed that the most powerful RF bands are GSM 900, GSM 1800, and 3G at 2.1 GHz with power levels in the range of -50 dBm (10 nW) to -15 dBm (31 μW) [22]. The heatsink antenna in this work is designed to harvest from all these three frequency bands simultaneously. The available space for antennas is limited to the outer walls of the TEH's body. The heatsink antennas needed to be placed on each face of the outer wall such that they cover the surface area of the TEs to efficiently boost the energy collected by the TEH (in our case this area is 80 mm $\times$ 80 mm, as shown in Fig. 1(a)).

As far as the antenna topology is concerned, a differential wire antenna is a better choice because, 1) it has no ground plane, so we do not need to embed another metal layer or suffer from complicated feed between the antenna and the ground plane, 2) it is easier to integrate the heatsink fins on a simple wire antenna (as shown later in the design section), 3) an all-around radiation pattern is preferred for the energy harvesting application, which can be obtained from the typical omnidirectional radiation pattern of a wire antenna.

B. DESIGN EVOLUTION OF THE HEATSINK ANTENNA

We start with the typical V type dipole antenna design, with the two legs occupying the two adjacent side faces of the TEH box. A V antenna is a specific type of dipole where the angle (α) between its legs can be controlled to achieve a higher directional beam and reduce the side lobes, as shown in Fig. 4(a). The optimum included angle (α) can be calculated by using (5) to achieve the highest directivity when the V antenna is in air [23]. The calculated optimum angle is 88.2°, which is close to 90°. Maximum directivity is also achieved at $\alpha = 90°$ for the V antenna when it is placed on the body of the TEH, as shown in Fig. 4(b). Therefore,

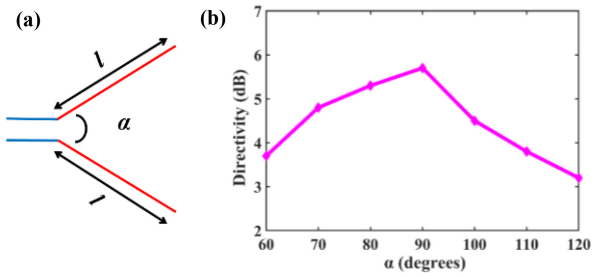

FIGURE 4. (a) Schematic of the V antenna (b) Directivity of the V antenna on the TEH as a function of angle (α) between the legs of the V antenna.

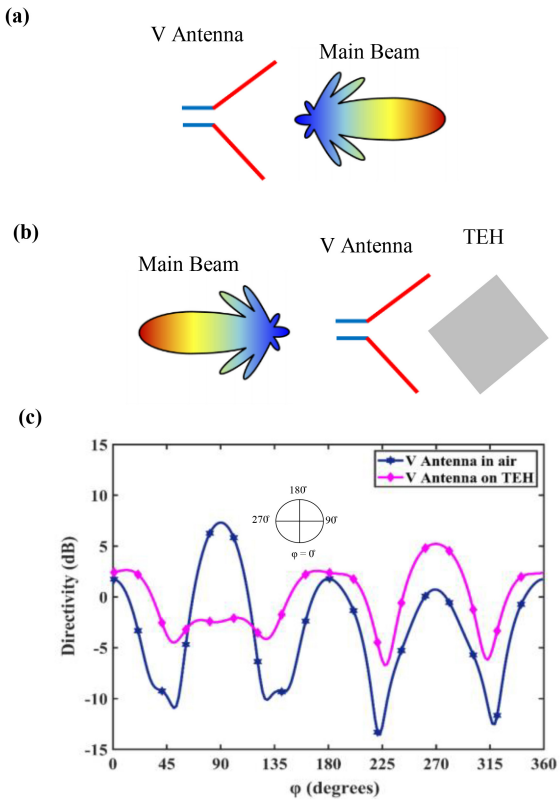

FIGURE 5. (a) V antenna in air with maximum directivity toward the inner angle between the legs (b) V antenna on the TEH with maximum directivity toward the ambient environment (c) Directivity of the V antennas in air and on the TEH as a function of azimuthal angle (φ).

in this work, the angle between the legs is fixed at 90°.

$$a = \begin{cases} -149.3\left(\frac{l}{\lambda}\right)^3 + 603.4\left(\frac{l}{\lambda}\right)^2 - 809.5\left(\frac{l}{\lambda}\right) + 443.6, \\ for\ 0.5 \le \left(\frac{l}{\lambda}\right) \le 1.5 \\ 13.39\left(\frac{l}{\lambda}\right)^2 - 78.27\left(\frac{l}{\lambda}\right) + 169.77, \\ for\ 1.5 \le \left(\frac{l}{\lambda}\right) \le 3 \end{cases} \quad (5)$$

For V antennas in air, the maximum directivity is toward the inner angle between the legs, as shown in Fig. 5(a). This direction is undesirable in our case as it is directed toward the body of the TEH and not the ambient environment. However, when the antenna is placed on the body of the TEH, the metallic parts of the TEH serve as a reflector providing maximum directivity toward the half-plane of the ambient

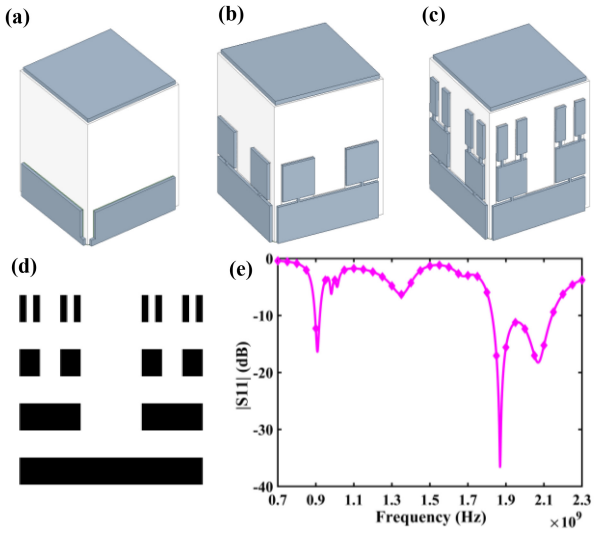

FIGURE 6. Cantor fractal antenna (a) 1st iteration (b) 2nd iteration (c) 3rd iteration (d) Cantor fractal schematic (e) Reflection coefficient of the 2D flat antenna.

environment, shown in Fig. 5(b), which is confirmed by the simulations as well as the measurements. Fig. 5(c) shows that when the V antenna is in air, its maximum directivity is in the direction where $\varphi = 90°$. However, when the V antenna is placed on the body of the TEH, its maximum directivity is in the direction where $\varphi = 270°$, which is in the direction of the ambient environment. A near-omnidirectional radiation pattern is preferred to capture most of the available ambient power, therefore, a second identical antenna is placed symmetrically on the remaining two adjacent side faces.

The 90° V antenna, shown in Fig. 6(a), operates on a single band (2.1 GHz). A single-band V antenna is evolved into triple-band antenna using the concept of fractals, widely used in designing multi-band and wideband antennas. Fractals are designed by an iterative process of copying self-repetitive scaled-down structures in a deterministic or random manner [23]. Each additional iteration of fractals introduces new current paths that can be tuned to achieve multi-band antenna performance. A Cantor fractal is used for this work due to its rectangular shape that could be used as a baseplate for the fins of the heatsink antenna. A Cantor fractal is obtained through a pattern where the first rectangular part is copied and divided into three equal rectangular pieces, and the middle one is deleted, as shown in Fig. 6(d). The length of the first iteration is 82 mm, which is the wavelength at 2.1 GHz on the ABS dielectric. Longer current paths equivalent to 1.8 GHz and 0.9 GHz wavelengths are attained with the 2nd and 3rd iterations, as shown in Fig. 6(b–c). The width of the rectangular parts is constrained by the upper limit of 110 mm/3 = 36.7 mm and lower limit of 80 mm/3 = 26 mm, where 110 mm is the height of the TEH and 80 mm is the length of the TE, in order to cover most part of the TE's surface area, as shown in Fig. 1(a). Small separations between the iterations are used to efficiently match the antenna for the three required

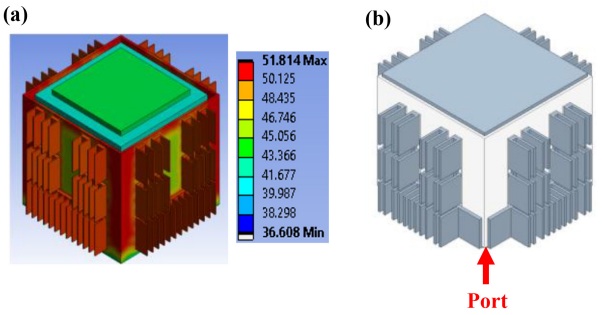

FIGURE 7. Model of the ambient energy harvester with heatsink antennas in (a) Ansys Fluent (b) Ansys HFSS.

frequencies. Fig. 6(e) shows the reflection coefficient of the 2D flat antenna on the body of the TEH, which is well-matched for the frequencies of interest (900 MHz, 1800 MHz and 2100 MHz). The antenna radiation efficiency is approximately ∼40% for the three frequencies, which is severely affected by the lossy body of the TEH.

C. DESIGN OF FINS FOR SIMULTANEOUS OPTIMIZATION OF HEAT TRANSFER AND EM RADIATION PERFORMANCES

The heat transfer characteristics of the fins have been studied in order to optimize the heat transfer as well as EM performance simultaneously during the heatsink antenna design. A heatsink is a device that enhances the heat transfer between a hot and a cold body by increasing the convection-active surface area [24]. Collected power from the TEH is directly proportional to the heat transfer coefficient, which, based on the simulations, is equal to h = 10 W/m^2·K in case of the flat TEH surface and h = 200 W/m^2·K in case of the optimized heatsink [21]. Parameters such as fins orientation, length, thickness and spacing between them are important from thermal performance perspective, however the dimensions of these parameters affect the antenna EM performance as well. Thus, these parameters have been studied in parallel through a computational fluid dynamics (CFD) simulator, the Ansys Fluent (model shown in Fig. 7(a)), as well as in Ansys HFSS, (model shown in Fig. 7(b)).

1) FIN ORIENTATION

For ambient energy harvesting, vertically oriented fins, shown in Fig. 8(a), are more effective than the horizontally oriented fins, shown in Fig. 8(b), because they are better aligned with the flow of the natural convection where hot/cold air moves up/down due to different densities and is directed by gravity. So, for natural convection (which occurs in ambient energy harvesting), it is known that vertically oriented fins perform much better (more than twice in terms of efficiency [25]) than horizontally oriented fins. Thus, no compromise is considered from the EM performance perspective and vertically oriented fins are used for this work.

2) BASEPLATE LENGTH

The length of the heatsink baseplate, shown in Fig. 8(c), must be sufficient to cover the surface area of the TE (80 mm × 80 mm) for optimal heat transfer. On the other hand, this length also determines the resonance frequency of the antenna. If we consider the typical λ/2 length for a dipole (at 2.1 GHz), the physical length of the baseplate must be 20 mm, however, this is insufficient for optimal heat transfer. Thus, we use a dipole with a leg length of λ instead (82 mm for 2.1 GHz). Through this choice, we get the best of both worlds, i.e., optimized EM performance for the antenna as well as the best heat transfer for the proposed TEH.

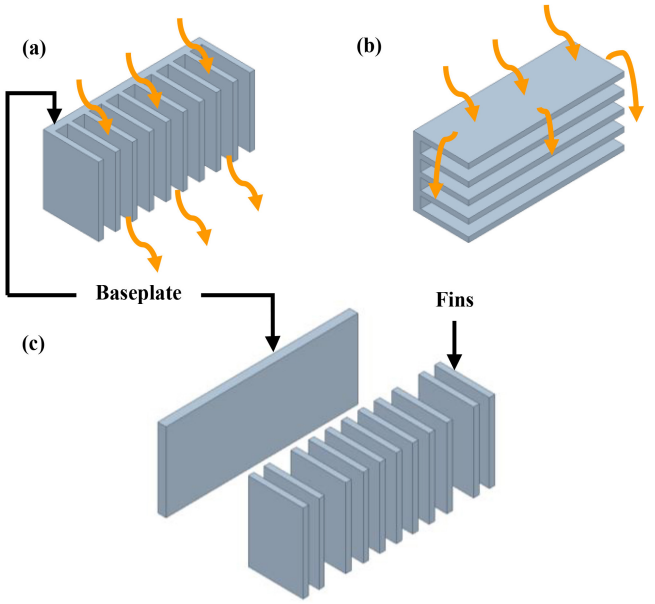

FIGURE 8. (a) Vertically oriented fins (b) Horizontally oriented fins (c) Exploded view of the vertically oriented heatsink: baseplate and fins.

3) FIN LENGTH

The heat transfer rate of a fin, shown in Fig. 9(a), is given by (6) [24].

$$q_f = M\tanh mL \tag{6}$$

where L is the length of the fin and M and m are constants that depend on the fin material, fin dimensions (other than the length), and the ambient environmental conditions. The relationship between the heat transfer rate and length of the fin is a hyperbolic tangent (tanh L) function (shown in Fig. 9(b)), which theoretically has its maximum value when L is infinity. However, in practical scenario the value of this function saturates for a certain fin length because the temperature gradient decreases along the fin length. This occurs due to the continuous convection heat losses from the initial part of the fin that is closer to the baseplate. This conclusion has been verified for the heatsink in the Ansys Fluent simulator, as shown in Fig. 9(c). It can be seen that the heat transfer rate saturates when the length of the fin exceeds 20 mm. This integration of a single fin enhances the heat transfer performance by 40% compared to the 2D structure (without fins). Additional fin length negligibly affects the heat transfer performance, although it makes the heatsink antenna heavier, bulkier, and more expensive.

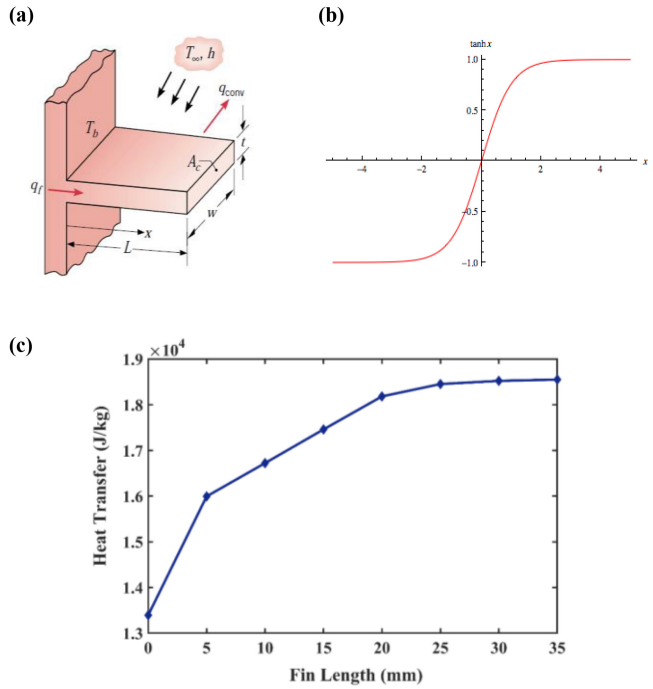

FIGURE 9. (a) Schematic of a fin [16] (b) Hyperbolic tangent function (tanh x) (c) Heat transfer per unit mass as a function of fin length.

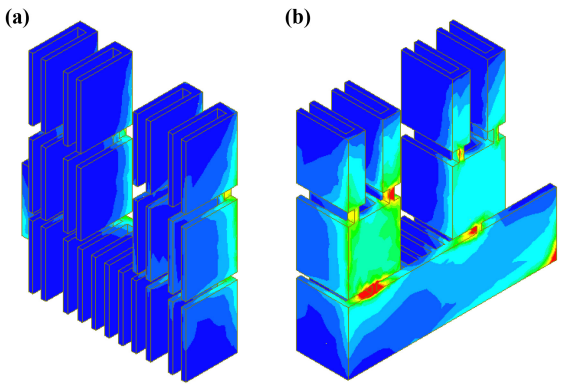

FIGURE 10. Current distribution on the heatsink antenna (a) Front-isometric view (b) Back-isometric view.

From the antenna's radiation perspective, integrating the fins with the 2D flat antenna has a kind of loading effect that shifts the resonance frequency to a lower frequency. This could also be explained by the increase in the effective antenna dimensions due to the additional length added by the fins. The current distribution on the antenna (Fig. 10) shows that the high currents are mainly concentrated on the base-plate of the heatsink antenna and inserting fins on top of the 2D antenna does not disturb the performance of the initial antenna significantly. Therefore, the rectangular baseplate length is reduced from 82 mm to 70 mm to compensate for the resonance shift. Though, the antenna is not covering the TE surface area fully and we compromised slightly regarding the optimal heat transfer, it is still covering a decent surface area (∼85%) and thus, the performance deterioration is not

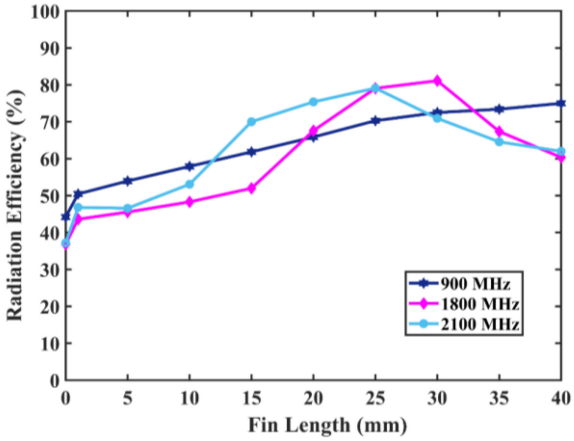

FIGURE 11. Antenna radiation efficiency as a function of fin length.

TABLE 2. Gain and radiation efficiency of the heatsink antenna.

Frequency	Heatsink antenna gain (dB)	Heatsink antenna radiation efficiency (%)
900 MHz	3.8	70.3
1800 MHz	4	79
2100 MHz	5.3	79.1

significant. This step is important for the antenna to operate at the right frequencies, thus, a compromise was required.

The antenna radiation efficiency versus the fin length is shown in Fig. 11 for the three frequencies. As shown, a fin length of 25 mm could be selected due to the best radiation efficiency performance for all three frequencies (∼80%). This is within the range of the optimal fin length for the best heat transfer performance (fin length above 20 mm), thus no compromise is required concerning the optimum fin length. It is noteworthy that the radiation efficiency doubled because of the integration of the fins compared to the 2D antenna, in addition to the 40% enhancement in heat transfer performance. The antenna performance enhancement could also be assessed through its gain, as shown in Table 2 for all three frequencies. As it can be observed, the gain of the heatsink antenna is improved by ∼3–4 dB compared to the 2D flat antenna. The increase in radiation efficiency could be explained by a large part of the radiating surface (the fins) being completely in air (away from the lossy dielectric), so there is significant decrease in the dielectric losses. The main contributor of the dielectric losses is TE as shown in Table 1. In case if TEs have no dielectric loss, the antenna radiation efficiency of the heatsink antenna would be 85%, 95% and 97% at 900 MHz, 1800 MHz and 2100 MHz frequencies respectively, that are reasonable and expected values for bulk metallic antennas. Though, there will be some increase in the conductor losses but overall this is not the dominant factor considering the lossy dielectric involved in this design. This increase in the radiation efficiency is also the cause of the increased gain, though, the directivity does increase slightly but it has negligible effect on the antenna gain.

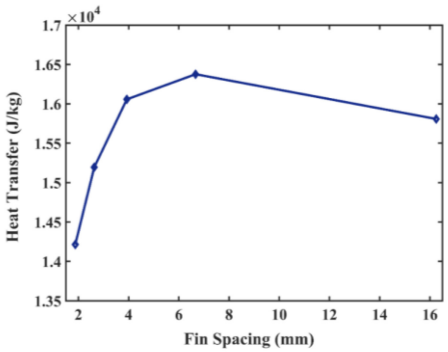

FIGURE 12. Heat transfer per unit mass as a function of fin spacing.

4) FIN THICKNESS

The fin effectiveness is the ratio of the heat transfer rate of the surface with the fins to the heat transfer rate of the surface without the fins [18]. It can be calculated using (7).

$$\varepsilon_f = \sqrt{kP}/hA_c \tag{7}$$

where k is the conductivity of the fin metal, P is the perimeter of the fin cross-section, A_c is the area of the fin cross-section, (shown in Fig. 9(a)), and h is the convection coefficient.

Based on (8), the fin effectiveness can be increased by increasing the ratio P/A_c:

$$\frac{P}{A_c} = \frac{2(w+t)}{w\ t} \approx \frac{2}{t} \tag{8}$$

assuming that $w >> t$. Therefore, by decreasing the thickness of the fin, the ratio of the fin's cross-section perimeter to its cross- area can be increased. Thus, thin fins are preferred from the heat transfer perspective. From the antenna's radiation perspective, the fin thickness has little to no effect since most of the stronger currents are on the baseplate near the feed point (Fig. 10). Therefore, heat transfer optimization was prioritized regarding the thickness of the fins. In our case, the minimum fin thickness is dictated by the manufacturing resolution, which is 2 mm for the computer numerical control (CNC) machine used in this work and thus this thickness is selected for our work.

5) SPACING BETWEEN THE FINS (NUMBER OF FINS)

Increasing the number of fins simply increases the convection-active surface area. From that perspective, tightly spaced fins are preferred because more number of fins can be accommodated in a given area. However, the spacing between the fins must not be decreased to a value where the air flow between the fins is significantly disrupted [24]. Ansys Fluent simulations have been conducted to determine the optimum fin spacing, where the natural air flow is imitated with a convection coefficient of h = 10 W/m^2·K [21]. Fig. 12 shows that the optimal spacing between the fins is between 4 mm and 8 mm for our specific environmental conditions. If the spacing is less than 4 mm, the performance decreases due to the blocked and disrupted air flow, however, if the spacing exceeds 8 mm, the performance starts to deteriorate because of the lower number of fins that could be accommodated on the fixed length baseplate.

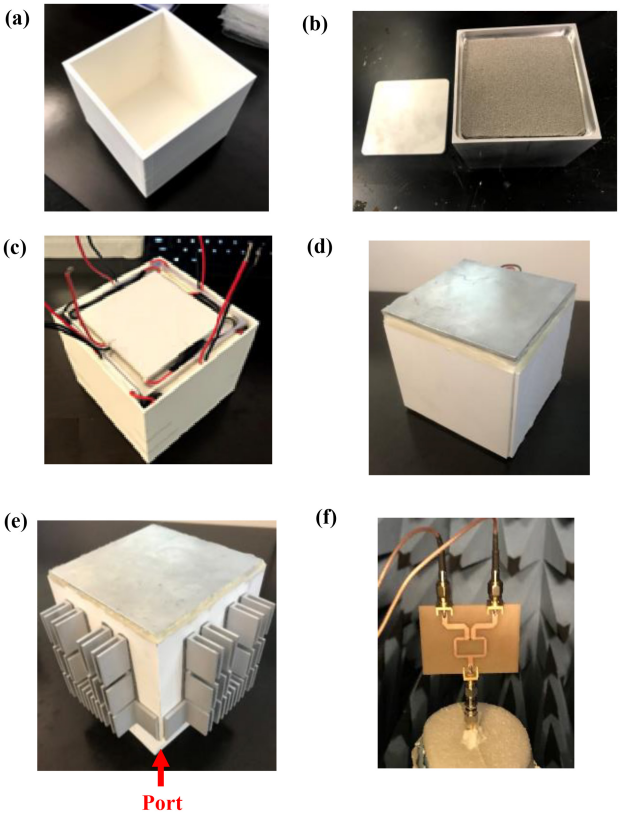

FIGURE 13. (a) 3D printed ABS box (b) Aluminum (Al) box filled with nickel (Ni) foam and eicosane (E) (c) Al box and 20 thermoelectric (TE) units placed inside the ABS box (d) Fabricated TEH (e) Fabricated heatsink antenna attached to the TEH (f) 3 dB power splitter.

From the EM radiation perspective, Fig. 10 shows that the area around the fins has low currents compared to the baseplate of the heatsink. Thus, fin spacing negligibly affects the antenna performance. Therefore, values extracted from the heat transfer optimization could be used.

6) MATERIAL CHOICE

Based on (4), it can be seen that the fin effectiveness could be increased by selecting a material with high thermal conductivity. From the EM radiation perspective, a material with high electrical conductivity must be selected as well, since it affects the antenna radiation efficiency. Al is chosen as a heatsink material due to its decent electrical conductivity ($\sigma = 3.7 \times 107$ S/m) and decent thermal conductivity (k = 240 W/m·K), lower cost, and easier manufacturability compared to other options.

IV. HEATSINK ANTENNA FABRICATION AND CHARACTERIZATION

The following materials and components are required to fabricate the TEH: 1) nickel (Ni) foam and a bottle of eicosane (E), 2) an Al box and Al inner and outer lids, 3) a 3D printed ABS box, shown in Fig. 13(a), and 4) 20 TEs. First, the Al box is filled with the Ni/E mixture, shown in

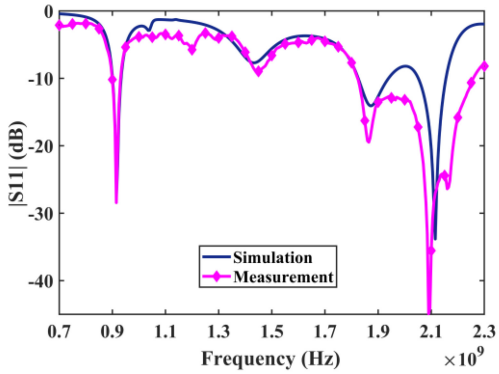

FIGURE 14. Reflection coefficient of the heatsink antenna.

Fig. 13(b), and the Al lid is placed on top. Twenty TEs (4 TEs on each 5 sides) and the Al box are placed inside the ABS box, as shown in Fig. 13(c). The TEs are connected in series to have one output that comes out from the drilled hole at the bottom of the TEH. Finally, the outer Al lid is placed and sealed on top of the TEH, as shown in Fig. 13(d). Heatsink antennas, made of Al, are manufactured through the CNC machine and assembled on the body of the fabricated TEH, as shown in Fig. 13(e). Thermally conductive and adhesive pads are used to strongly attach the heatsink antennas to the body of the TEH.

Fig. 14 shows the measured reflection coefficient (|S11|) of a single heatsink antenna that has a decent match with the simulation results at 900 MHz, 1800 MHz and 2100 MHz frequency bands. The other identical antenna has a similar performance in terms of matching and impedance bandwidth. These measurement results validate the assumptions made during the material characterization of the TEH.

The radiation performance is measured in two steps. Firstly, two symmetrical antennas are characterized separately when only one antenna is excited in the anechoic chamber. Fig. 15 shows the E and H planes of the radiation patterns for one separate antenna. In the second step, both antennas are excited through the 3 dB power splitter, as shown in Fig. 13(f), and the overall radiation pattern is measured. Fig. 16 shows the E and H planes of the radiation pattern for the simulation and measurements. The simulation and measurement results have decent match with each other at the 900 MHz, 1800 MHz and 2100 MHz frequency bands. However, some small discrepancies are observed. This might be caused by the extra radiation from the 3 dB power splitter as well as the flexible cables used inside the anechoic chamber but not in the simulation model. The antenna system has 3.8 dB, 4 dB and 5.3 dB of gain at 900 MHz, 1800 MHz and 2100 MHz frequencies respectively, and an acceptable all-around radiation pattern.

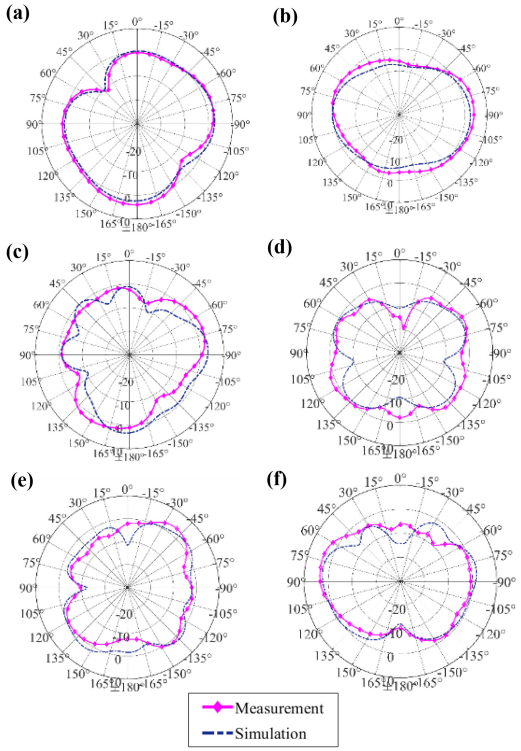

FIGURE 15. Measured and simulated radiation patterns of the heatsink antenna (a) H plane at 900 MHz (b) E plane at 900 MHz (c) H plane at 1800 MHz (d) E plane at 1800 MHz (e) H plane at 2100 MHz (f) E plane at 2100 MHz.

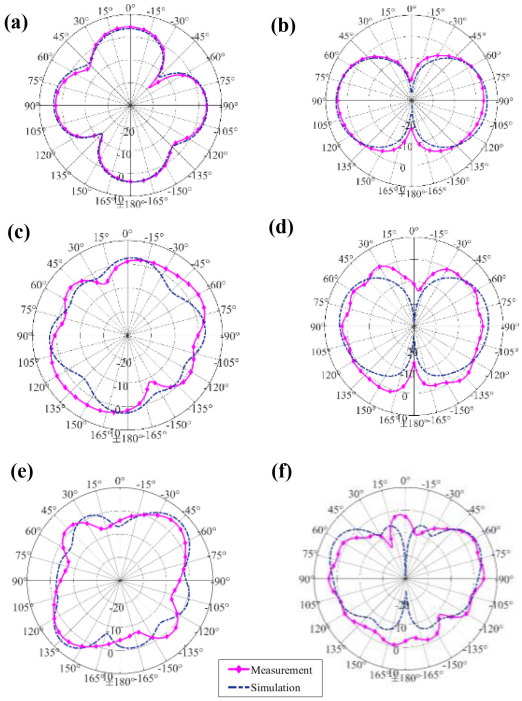

FIGURE 16. Measured and simulated radiation patterns of two heatsink antennas (a) H plane at 900 MHz (b) E plane at 900 MHz (c) H plane at 1800 MHz (d) E plane at 1800 MHz (e) H plane at 2100 MHz (f) E plane at 2100 MHz.

V. RECTIFIER CIRCUIT AND TRIPLE-BAND MATCHING NETWORK

Since the available RF energy in the ambient environment is relatively small, in the microwatt range, a series single diode rectifier is designed as it minimizes the potential losses of the components of the rectifier circuit. A Schottky diode SMS 7630-079 from Skyworks is selected for this work due to its low turn-on voltage [26]. Though the diode performance is

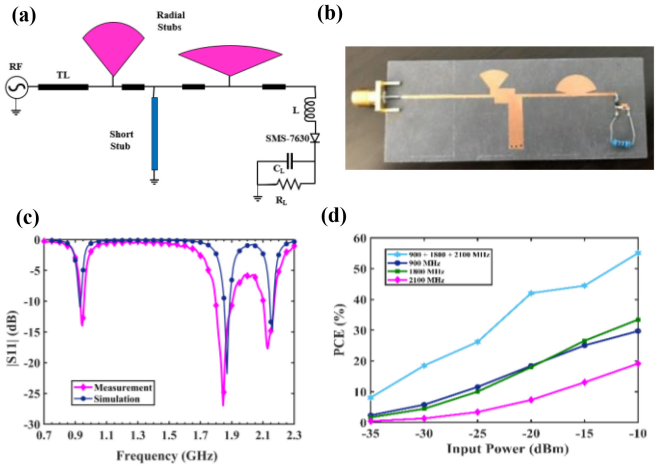

FIGURE 17. (a) Schematic of the rectifier with the triple-band matching network (b) Fabricated rectifier with the triple-band matching network (c) Reflection coefficient of the rectifier with the triple-band matching network (d) PCE of the rectifier as a function of input power for different frequency bands.

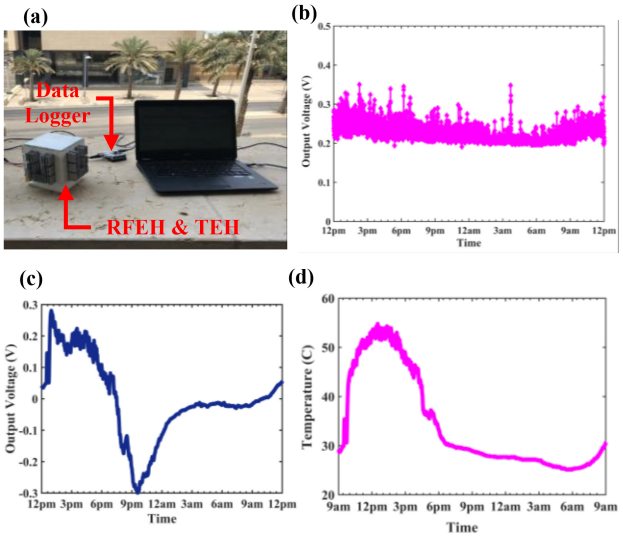

FIGURE 18. (a) Field testing setup (b) Output voltage of the RFEH (c) Output voltage of the TEH (d) Temperature fluctuations in 24 hours.

theoretically temperature dependent, datasheet of the diode in the Skyworks website ensures stable operation between −65°C and 150°C temperature range where the ambient environment fluctuations are well within this range. The input impedance of the rectifier diode must be matched to the heatsink antenna impedance (50 Ω) at three frequencies simultaneously. This is a challenging task since the diode impedance is a function of frequency as well as input power.

The triple-band matching network (matched at −20 dBm) is designed using the Keysight Advanced Design System (ADS). As shown in Fig. 17(a), it consists of two radial stubs and one short stub whose dimensions are accurately tuned to match the diode impedance at three frequencies simultaneously. A rectifier circuit with a triple-band matching network is fabricated on a Roger/Duroid 5880 substrate due to its low dielectric loss 0.0009 (Fig. 17(b)). A circuit board is packaged inside a 3D printed ABS box, which is then placed at the bottom of the TEH body. Characterization results of the rectifier circuit with the matching network are shown in Fig. 17(c–d) in terms of matching (measured at −20dBm) and the PCE [22]. As shown in Fig. 17(c) impedance of the diode rectifier is well matched to the 50 Ω antenna impedance at frequencies of interest for both simulation and measurement. In terms of rectification, Fig. 17(d) shows the measured results where the triple-band harvesting enhances the PCE significantly compared to the single-band harvesting. For example, at −20 dBm, PCE of the rectifier increases from 5% and 15% for single bands up to 40% for triple-band harvesting.

VI. FIELD TESTING

Field testing has been conducted in a university campus area to measure the harvested RF energy and thermal energy in a real environment. Fig. 18(a) shows the field testing setup where the multi-source energy harvester with heatsink antennas is connected to the laptop through data loggers from Picotech. The measurement has been conducted for 24 hours by recording the output voltage every 10 seconds separately for the RFEH and the TEH. Fig. 18(b) shows the output voltage of the RFEH, which is constant at around 250 mV throughout the whole day. This is equivalent to 6.25 μW of output power across a 10 kΩ resistive load. Fig. 18(c) shows the output voltage of the TEH throughout the 24 hours, measured across the 100 Ω load resistance to achieve maximum power transfer.s1 Unlike the RFEH's output, it is not constant since it closely follows the temperature fluctuations during the day as shown in Fig. 18 (d). A negative output voltage represents a night time when the ambient temperature is lower than the temperature of the PCM (37°C).

The time-averaged output power of the TEH without heatsink fins is 13.6 μW, which has been improved by 2.3 times (∼130%) when the heatsink fins are integrated.

VII. CONCLUSION

In this paper, we presented a dual-function triple-band (900 MHz, 100 MHz and 2100 MHz) heatsink antenna for smart integration of the RFEH and the TEH. The antenna is designed through co-optimization of the EM radiation performance using Ansys HFSS and the heat transfer performance of the heatsink fins using Ansys Fluent. An antenna performance improvement is achieved in terms of radiation efficiency (from ∼40% to ∼80%), resulting in gain improvement by ∼3–4 dB compared to the 2D flat version of the antenna (without fins). The RFEH collected a constant ∼250 mV (6.25 μW across 10 kΩ load) output voltage throughout the 24-hour active field testing. Moreover, ∼130% more power (increase in time-averaged power from 13.6 μW to 31.3 μW) has been collected by the TEH with optimized fins compared to the TEH without fins.

REFERENCES

[1] "Internet of Things: Number of Connected Devices Worldwide 2015–2025." Statista Research Department. Statista.com. 2019. [Online]. Available: https://www.statista.com/statistics/471264/iot-number-of-connected-devices-worldwide/

[2] M. F. Farooqui, M. A. Karimi, K. N. Salama, and A. Shamim, "3D-printed disposable wireless sensors with integrated microelectronics for large area environmental monitoring," *Adv. Mater. Technol.*, vol. 2, no. 8, 2017, Art. no. 1700051.

[3] M. F. Farooqui and A. Shamim, "Low cost inkjet printed smart bandage for wireless monitoring of chronic wounds," *Sci. Rep.*, vol. 6, Jun. 2016, Art. no. 28949.

[4] Z. Su, K. Klionovski, R. M. Bilal, and A. Shamim, "A dual band additively manufactured 3-D antenna on package with near-isotropic radiation pattern," *IEEE Trans. Antennas Propag.*, vol. 66, no. 7, pp. 3295–3305, Jul. 2018.

[5] J. Singh, R. Kaur, and D. Singh, "Energy harvesting in wireless sensor networks: A taxonomic survey," *Int. J. Energy Res.*, vol. 45, no. 1, pp. 118–140, 2021.

[6] A. Bakytbekov *et al.*, "Multi-source ambient energy harvester based on RF and thermal energy: Design, testing, and IoT application," *Energy Sci. Eng.*, vol. 8, no. 11, pp. 3883–3897, 2020.

[7] S. Shen, Y. Zhang, C. Chiu, and R. Murch, "A triple-band high-gain multibeam ambient RF energy harvesting system utilizing hybrid combining," *IEEE Trans. Ind. Electron.*, vol. 67, no. 11, pp. 9215–9226, Nov. 2020.

[8] U. Muncuk, K. Alemdar, J. D. Sarode, and K. R. Chowdhury, "Multiband ambient RF energy harvesting circuit design for enabling batteryless sensors and IoT," *IEEE Internet Things J.*, vol. 5, no. 4, pp. 2700–2714, Aug. 2018.

[9] Z. Liu, Z. Zhong, and Y. Guo, "Enhanced dual-band ambient RF energy harvesting with ultra-wide power range," *IEEE Microw. Wireless Compon. Lett.*, vol. 25, no. 9, pp. 630–632, Sep. 2015.

[10] C. H. P. Lorenz, S. Hemour, W. Liu, A. Badel, F. Formosa, and K. Wu, "Hybrid power harvesting for increased power conversion efficiency," *IEEE Microw. Wireless Compon. Lett.*, vol. 25, no. 10, pp. 687–689, Oct. 2015.

[11] X. Gu, S. Hemour, and K. Wu, "Integrated cooperative radiofrequency (RF) and kinetic energy harvester," in *Proc. IEEE Wireless Power Transf. Conf. (WPTC)*, 2017, pp. 1–3.

[12] Y. Zhang, S. Shen, C. Y. Chiu, and R. Murch, "Hybrid RF-solar energy harvesting systems utilizing transparent multiport micromeshed antennas," *IEEE Trans. Microw. Theory Techn.*, vol. 67, no. 11, pp. 4534–4546, Nov. 2019.

[13] L. Guo, X. Gu, P. Chu, S. Hemour, and K. Wu, "Collaboratively harvesting ambient radiofrequency and thermal energy," *IEEE Trans. Ind. Electron.*, vol. 67, no. 5, pp. 3736–3746, May 2020.

[14] M. Virili *et al.*, "Performance improvement of rectifiers for WPT exploiting thermal energy harvesting," *Wireless Power Transf.*, vol. 2, no. 1, pp. 22–31, 2015.

[15] L. Covert and J. Lin, "Simulation and measurement of a heatsink antenna: A dual-function structure," *IEEE Trans. Antennas Propag.*, vol. 54, no. 4, pp. 1342–1349, Apr. 2006.

[16] J. J. Casanova, J. A. Taylor, and J. Lin, "Design of a 3-D fractal heatsink antenna," *IEEE Antennas Wireless Propag. Lett.*, vol. 9, pp. 1061–1064, 2010.

[17] A. Alnukari, Y. Mahe, S. Toutain, and Y. Scudeller, "Microstrip heatsink antenna cooled with sapphire layer for integrated RF transmitters," in *Proc. 6th Eur. Conf. Antennas Propag. (EUCAP)*, 2012, pp. 1263–1266.

[18] J. Ge and G. Wang, "A heatsink integrated antenna with controllable electromagnetic and thermal performance," in *Proc. IEEE Int. Symp. Antennas Propag. North Amer. Radio Sci. Meeting*, 2020, pp. 419–420.

[19] J. Qian, M. Tang, Y.-P. Zhang, and J. Mao, "Heatsink antenna array for millimeter-wave applications," *IEEE Trans. Antennas Propag.*, vol. 68, no. 11, pp. 7664–7669, Nov. 2020.

[20] I. Dincer, *Comprehensive Energy Systems*. Amsterdam, The Netherlands: Elsevier, 2018.

[21] A. L. Cottrill *et al.* "Persistent energy harvesting in the harsh desert environment using a thermal resonance device: Design, testing, and analysis," *Appl. Energy*, vol. 235, pp. 1514–1523, Feb. 2019.

[22] A. Bakytbekov, T. Q. Nguyen, C. Huynh, K. N. Salama, and A. Shamim, "Fully printed 3D cube-shaped multiband fractal rectenna for ambient RF energy harvesting," *Nano Energy*, vol. 53, pp. 587–595, Nov. 2018.

[23] C. Balanis, *Antenna Theory, Analysis and Design*. Hoboken, NJ, USA: Wiley, 2005.

[24] F. P. Incropera, "Heat transfer from extended surfaces," in *Fundamentals of Heat and Mass Transfer*, 6th ed. Hoboken, NJ, USA: Wiley, 2011.

[25] "Comparing Naturally Cooled Horizontal Baseplate Heat Sinks With Vertical Baseplate Heat Sinks." 2004. [Online]. Available: http://www.thermalsoftware.com/vert_vs_horz_sink.pdf

[26] "Surface-Mount Mixer and Detector Schottky Diodes." Skyworks. [Online]. Available: https://www.skyworksinc.com/-/media/SkyWorks/Documents/Products/201-300/Surface_Mount_Schottky_Diodes_200041AE.pdf